Bioinspired carrier-free peptide conjugated BF$_2$-oxasmaragdyrin dye-based nano self-assemblies: a photostable NIR cancer theragnostic agent

Kandala Laxman [1,2,3], B. Pradeep K. Reddy [4], Sumit K. Mishra[5,6], Andrea Robinson [3], Abhijit De [5,6], Rohit Srivastava [4] and Mangalampalli Ravikanth [2]

Abstract
Photothermal therapy (PTT) has attracted great interest in cancer treatment, and the quest for potential organic photothermal agents is underway owing to the nonbiodegradable nature and chronic toxicity of existing inorganic nanomaterials. Organic material-based nanoformulations with good photothermal and fluorescence properties in the near-infrared (NIR-I) window are scarce. However, porphyrins are one category of biocompatible systems that are advantageous for photothermal therapy but are currently based in the visible region, causing limited depth of tissue penetration and leading to compromised photothermal and near-infrared fluorescence (NIRF) imaging applications. To overcome these limitations, we report the synthesis of L,L-diphenylalanine conjugated BF$_2$-oxasmaragdyrin (FF-BSC) and the fabrication of monodispersed spherical self-assemblies (FF-BSC NPs) using a USP class 3 solvent-water mixture. The resulting product exhibited excellent photostability (NIR exposure), multicycle photothermal efficacy, and NIR fluorescence. In vitro studies revealed good biocompatibility, efficient cellular internalization, and photothermal efficacy. Preclinical studies of these nano-self-assemblies demonstrated nontoxicity, efficient whole-body NIRF imaging, fractional passive tumor homing, and excellent photothermal tumor ablation potential. The absorbance and fluorescence of FF-BSC NPs in NIR-I make them suitable for theragnostic applications over existing porphyrins/inorganic nanomaterials for future clinical applications.

Introduction

There has been a rapid increase in the incidence of cancer and the associated mortalities worldwide. Cancer is the second leading cause of death, exceeded only by noncommunicable diseases, and it remains a major barrier to higher life expectancy globally[1]. Current cancer therapeutic modalities are often limited to surgery, chemotherapy, radiation therapy, and immunotherapy due to the heterogeneous nature of cancer. These therapeutic approaches are often associated with untoward side effects, and hence, improved novel alternatives are in high demand[2]. One such promising and widely studied approach is photothermal therapy (PTT). PTT is an exciting strategy owing to its minimal invasiveness, ease of operation, rapid treatment time, and quick patient recovery[3]. The success of PTT relies heavily on photothermal agents that convert light energy to localized heat and are being utilized for tumor ablation. To date, various materials have been screened for their application in PTT, including gold nanoparticles[4,5], graphene and graphene oxide[6,7], black phosphorus[8], palladium[9], copper sulfide[10], copper selenide[11], and molybdenum oxide[12]. The non-biodegradability and long-term toxicity of inorganic

Correspondence: Andrea Robinson (Andrea.Robinson@monash.edu) or
Abhijit De (ade@actrec.gov.in) or Rohit Srivastava (rsrivasta@iitb.ac.in) or
Mangalampalli Ravikanth (ravikanth@chem.iitb.ac.in)
[1]IITB-Monash Research Academy, Indian Institute of Technology Bombay,
Powai, Mumbai 400076, India
[2]Department of Chemistry, Indian Institute of Technology Bombay, Powai,
Mumbai 400076, India
Full list of author information is available at the end of the article
These authors contributed equally: Kandala Laxman, B. Pradeep K. Reddy,
Sumit K. Mishra

materials, however, are of grave concern. Though polymer-based materials have been developed and their photothermal potential evaluated[13–16], such materials often require complicated processing techniques.

The need to overcome these hurdles and develop efficient photothermal agents has propelled research towards organic dyes: materials possessing absorption/fluorescence in the first biological window (650–950 nm), possess excellent potential as NIRF imaging and/or therapeutic agents[17]. Hence, there is a growing need for dyes that can be easily prepared to absorb and emit strongly in the NIR region. To the best of our knowledge, there are a limited number of dyes that fluoresce in this region, which include cyanine dyes[18], squaraine dyes[19,20], BODIPY analogs[20,21], xanthenes[22], phthalocyanines, and a small selection of porphyrin derivatives[23,24].

One type of molecule that absorbs and emits in the NIR region is smaragdyrins, which belong to the class of expanded porphyrins. Smaragdyrins are 22π aromatic expanded pentapyrrolic macrocycles in which five pyrroles are connected by three *meso* carbons and two direct pyrrole-pyrrole bonds[25]. Chandrasekhar and coworkers reported the synthesis of stable *meso*-triaryl 25-oxasmaragdyrins in which one of the pyrrole rings of pentaazasmaragdyrin is replaced with a furan ring[26,27]. The 25-oxasmaragdyrins absorb and emit in the Vis-NIR region with moderate quantum yields and singlet state lifetimes. Recently, our group reported the synthesis of BF$_2$- and PO$_2$-complexes of 25-oxasmaragdyrins[28–30], which exhibit improved photophysical properties compared to those of freebase 25-oxasmaragdyrin, and the NIRF imaging potential has been demonstrated[31,32].

Recent studies suggest that NIR fluorescent dyes in conjugation with self-assembling small biomolecules/peptides would be of great utility[33]. The simple dipeptide diphenylalanine is a key motif in β-amyloid polypeptide, which is known for its ability to self-assemble with variable morphologies. The mechanism behind its formation of ordered hierarchical structures relies on π-π stacking of aromatic residues and hydrogen bonding with a peptide backbone[34]. Diphenylalanine-conjugated self-assemblies

of porphyrin[35] and phthalocyanine[36,37] were recently reported as anticancer agents. Herein, we report L,L-diphenylalanine-conjugated BF$_2$-oxasmaragdyrin self-assemblies to be effective theragnostic agents with good photothermal conversion efficiency (PCE) in comparison to the existing materials[38]. FF-BSC NPs were also found to be extremely stable under heat and physiological pH conditions. The L,L-diphenylalanine-conjugated BF$_2$-oxasmaragdyrin nanoparticles (FF-BSC NPs) exhibit absorption and emission in the NIR-I window with high photostability (>20 min of laser exposure), unlike commercially available NIR dyes such as ICG, IR780, and IR820, which quickly photobleach[39–41]. Owing to the low attenuation of NIR light by biological tissues, the FF-BSC NPs exhibited good NIR fluorescence and strong photothermal potential compared to other reported porphyrin-based nanoassemblies[35]. The formulation also exhibited excellent compatibility and photothermal efficacy under in vitro and in vivo conditions.

Results and Discussion
Synthesis and characterization

The target BF$_2$-25-oxasmaragdyrin-diphenylalanine conjugate **1** was prepared in a sequence of four steps (Scheme 1). The starting BF$_2$-25-oxasmaragdyrin **2**, containing a *p*-carboxymethylphenyl substituent at the *meso* position, was synthesized *via* a previously reported method[28,42]. Hydrolysis of ester **2** with LiOH in THF/H$_2$O provided a free carboxylic acid moiety at the *meso* position of BF$_2$-oxasmaragdyrin. Compound **3** was coupled to *C*-terminal protected L,L-diphenylalanine **4** in the presence of *N,N,N′,N′*-tetramethyl-*O*-(1*H*-benzotriazol-1-yl) uronium hexafluorophosphate (HBTU) and *N,N*-diisopropylethylamine (DIEA) in dichloromethane under an inert atmosphere for 8 h, followed by basic alumina column chromatographic purification to afford compound **5** as a green solid (55% yield). All intermediates were characterized by ^{1}H, ^{1}H-^{1}H COSY, ^{13}C, ^{11}B, ^{19}F NMR spectroscopy (Figs. S1–S19) and high-resolution mass spectrometry (HRMS) (Figs. S20–S22). In the last step, compound **5** was hydrolyzed to afford target compound **1**,
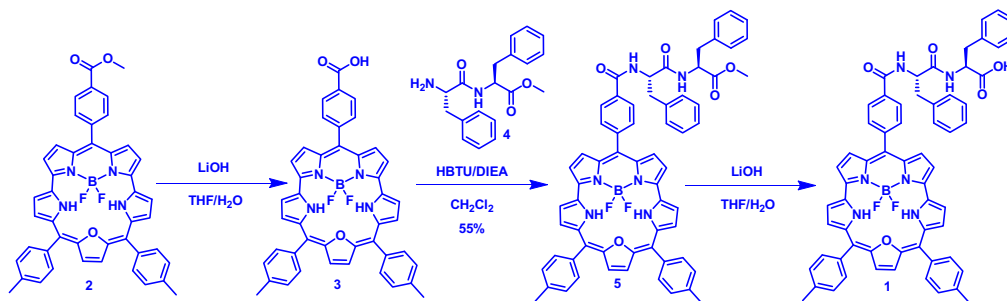
Scheme 1 Synthesis of L,L-diphenylalanine conjugated BF$_2$-oxasmaragdyrin 1.
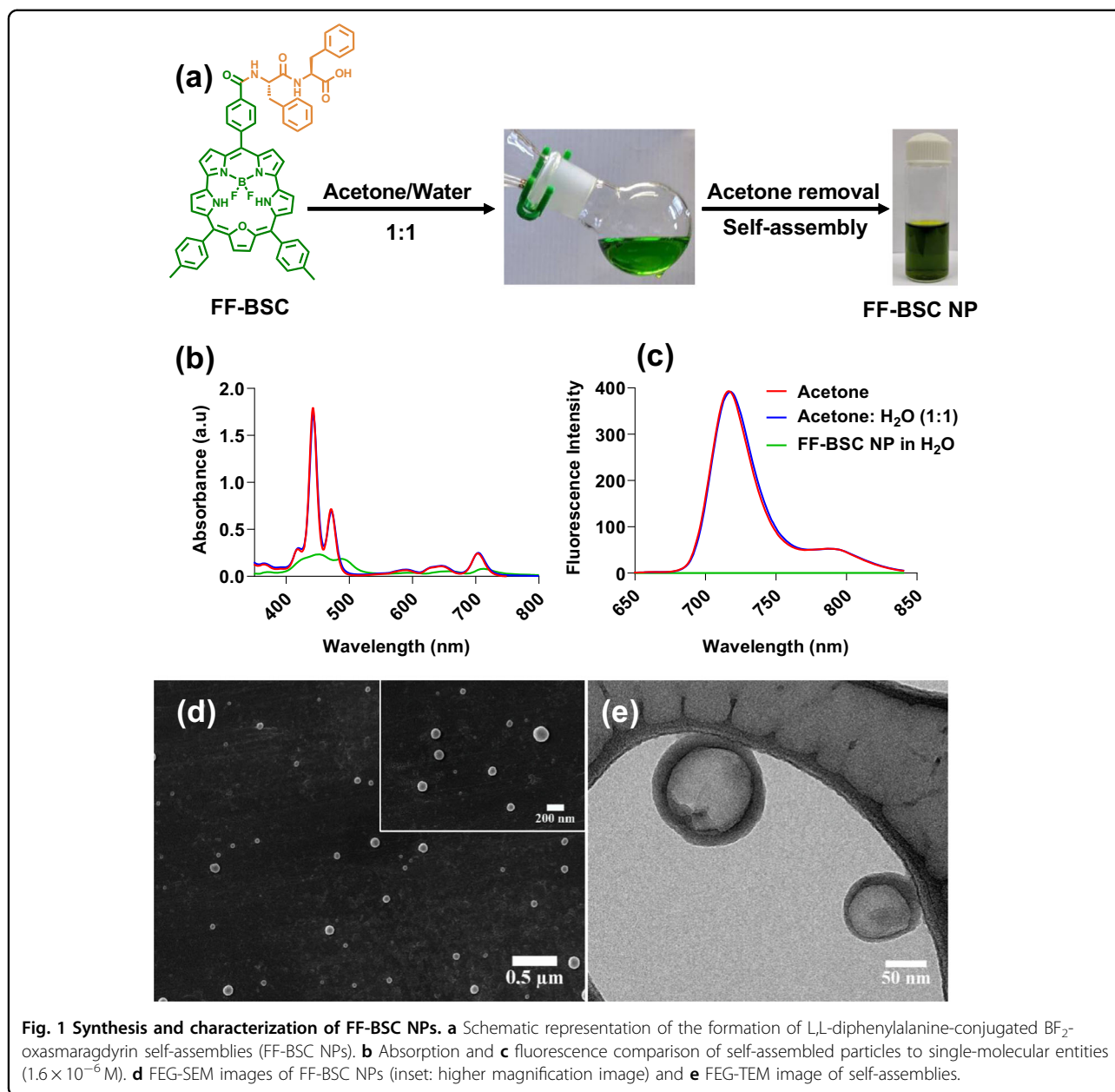
Fig. 1 Synthesis and characterization of FF-BSC NPs. a Schematic representation of the formation of L,L-diphenylalanine-conjugated BF_2-oxasmaragdyrin self-assemblies (FF-BSC NPs). **b** Absorption and **c** fluorescence comparison of self-assembled particles to single-molecular entities (1.6×10^{-6} M). **d** FEG-SEM images of FF-BSC NPs (inset: higher magnification image) and **e** FEG-TEM image of self-assemblies.

which was characterized by ^{1}H, ^{1}H-^{1}H COSY, ^{13}C, ^{11}B, ^{19}F NMR spectroscopy (Figs. S23–S27) and HRMS (Fig. S28). Absorption and fluorescence spectroscopic studies revealed that compound **1** possessed photophysical properties analogous to those of the parent molecule **2**.

Formation of self-assemblies

To prepare spherical self-assemblies, compound 1 was dissolved in different water-miscible solvents, including acetonitrile, hexafluoro-2-propanol, acetone, DMSO and was diluted with water. The solvent was then removed by either evaporation or dialysis. Particles with various morphologies (spheres/rods/tubes/mixtures) and sizes

were formed; aggregates were also observed under most conditions. An acetone-water mixture (1:1 ratio) yielded monodisperse nanoparticles with spherical morphology. The acetone was removed from the above solution under reduced pressure at 55 °C to obtain self-assembled spherical particles (FF-BSC NPs) (Fig. 1a). DLS analysis revealed that the FF-BSC NPs had a mean hydrodynamic diameter of 152.1 ± 13.7 nm and a polydispersity (PDI) of 0.09 ± 0.05. The nanoparticles had a zeta potential of -22 ± 5 mV. The FF-BSC NPs were characterized by spectroscopic and microscopic techniques (Fig. 1b–e, S29).

Significant changes were observed in the absorption and fluorescence spectra of compound **1** (Fig. 1b, c) after

Fig. 2 pH stability and lyophilization of FF-BSC NPs. Absorbance spectrum of FF-BSC NPs maintained at pH (**a**) 5.5, (**b**) 6.5, (**c**) 7.4; Fluorescence spectrum of FF-BSC NPs maintained at pH (**d**) 5.5, (**e**) 6.5, (**f**) 7.4. SEM images of FF-BSC NPs after lyophilization: (**g**) without cryoprotectant, (**h**) F-68 (0.5%) + sucrose (1%), and (**i**) F-68 (0.5%) + trehalose (1%).
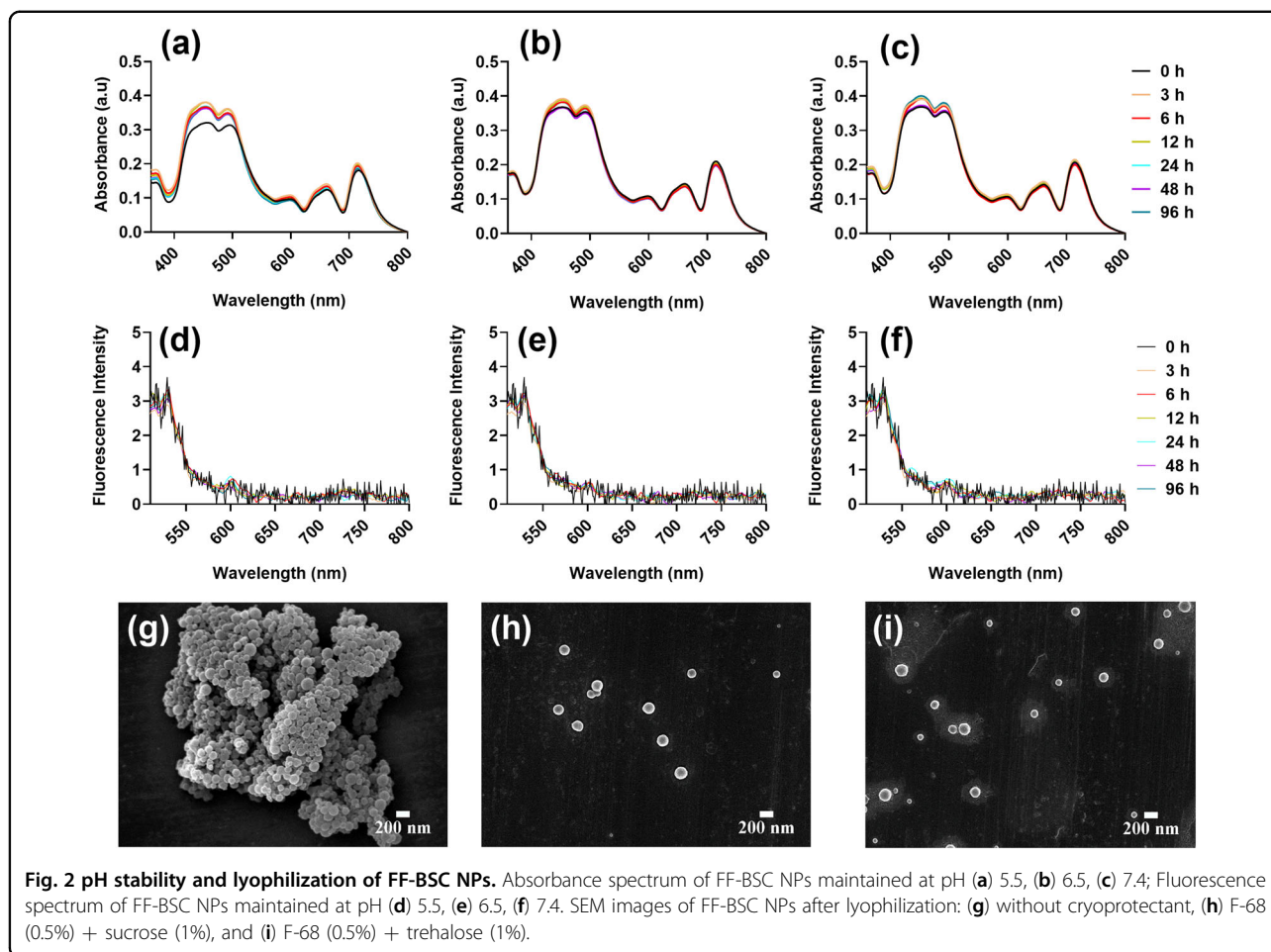
assembly into FF-BSC NPs. The absorption spectrum broadened, and the corresponding absorption coefficients were reduced. This was accompanied by significant quenching of fluorescence due to aggregation-induced quenching phenomena. To assess whether the nanoparticles were formed upon the addition of water to compound **1** in acetone or during the removal of acetone from the acetone-water mixture of compound **1**, the absorption and fluorescence spectra (Fig. 1b, c) of compound **1** were analyzed in acetone, acetone-water mixture (1:1 v/v) and water (post acetone removal). It was observed that there was no change in absorption and fluorescence spectra in acetone and the acetone-water mixture, indicating that the spectral differences arise from the molecular behavior of compound **1**. However, significant changes were observed in the absorption and fluorescence spectra of compound **1** due to the formation of self-assemblies upon removal of acetone from the acetone-water mixture. As acetone is evaporated from the solution, the hydrophobic nature of the BF_2-oxasmaragdyrin and diphenylalanine moieties creates a hydrophobic core due to π-π stacking, creating an external hydrophilic shell of carboxylic acid moieties with strong intermolecular hydrogen bonding with water. Furthermore, FEG-SEM and FEG-TEM analysis of the FF-BSC NPs revealed spherical nanoparticles with controllable morphology (Fig. 1d, e) and a diameter of 123 ± 33 nm (Fig. S30). The net result is the formation of stable, spherical, and monodispersed nanoparticles (FF-BSC NPs).

Stability studies
pH stability

The pH stability of the synthesized nanoparticles was evaluated under different physiological pH conditions (5.5, 6.5, and 7.4). The samples were withdrawn at predetermined time intervals, and the absorption and fluorescence spectra of the samples were recorded at different time points and did not exhibit any change (Fig. 2a–f). These results indicated that the nanoparticles were not disassembled and were stable across the pH range studied. Furthermore, SEM analysis of the samples after 96 h (Fig. S31) revealed spherical morphology, indicating the stability and non-dissociative nature of FF-BSC NPs.

Table 1 Mean hydrodynamic diameter (mean HDD) and PDI of FF-BSC NPs post lyophilization with various cryoprotectants.

S. No	Sample details	Mean HDD (nm)	PDI
1	Before lyophilization	152.10 ± 13.70	0.09 ± 0.05
2	No cryoprotectant	1415.0	0.707
3	Mannitol 1%	254.7	0.382
4	Mannitol 2.5%	278.4	0.401
5	Mannitol 5%	220.2	0.540
6	Sucrose 1%	428.2	0.782
7	Sucrose 2.5%	314.8	0.235
8	Sucrose 5%	165.5	0.075
9	Trehalose 1%	425.2	0.362
10	Trehalose 2.5%	323	0.251
11	Trehalose 5%	152.3	0.071
12	Pluronic F-68	294.8	0.279
13	F-68 0.5% + Mannitol 1%	171.7	0.382
14	F-68 0.5% + Mannitol 2.5%	237.4	0.404
15	F-68 0.5% + Mannitol 5%	163.9	0.233
16	F-68 0.5% +Sucrose 1%	162.2	0.071
17	F-68 0.5% +Sucrose 2.5%	162.4	0.029
18	F-68 0.5% +Sucrose 5%	167.7	0.024
19	F-68 0.5% +Trehalose 1%	178.4	0.127
20	F-68 0.5% +Trehalose 2.5%	175.7	0.099
21	F-68 0.5% +Trehalose 5%	172.4	0.099

Lyophilization

To enhance the storage stability of FF-BSC NPs, the sample was subjected to lyophilization. Three different cryoprotectants (sucrose, mannitol and trehalose) at three different concentrations (1%, 2.5%, 5% w/w) were studied in the presence/absence of poloxomer 188 (F-68). It was observed that the samples containing the cryoprotectants were readily reconstituted with Milli-Q. The DLS analysis revealed that sucrose and trehalose were effective in mitigating lyophilization stress. This effect was more pronounced in the presence of F-68, indicating the synergistic effect between the cryoprotectants and F-68[43], as shown in Table 1. Furthermore, SEM images of sucrose and trehalose lyophilized samples revealed distinct spherical nanoparticles, whereas the sample lyophilized without any cryoprotectant exhibited large aggregates (Fig. 2g–i).

Photothermal transduction studies
Photothermal transduction

The FF-BSC NPs exhibited good photothermal properties upon irradiation with a 750 nm laser. Evaluation of the photothermal transduction potential of a material provides the relationship between temperature rise and laser irradiation. The response surface methodology (RSM) approach could be used to identify the interactions among the factors. The photothermal transduction potential of the nanoparticles was evaluated by constructing a central composite design (CCD) using three independent variables, i.e., sample concentration, laser power, and laser irradiation time. The design layout, along with the independent and dependent variables, is provided in Table S1, and the experimental results are tabulated in Table S2. A quadratic model was selected ($p = 0.0025$), and the ANOVA of the chosen model revealed the model significant ($p < 0.0001$) and lack of fit insignificant ($p = 0.9433$), as shown in Table S3. Furthermore, the diagnostic plots did not reveal any abnormalities. The coded equation for the model is provided below:

$$Y = + 54.21 + 3.65A + 5.64B + 6.02C + 0.35AB + 0.97AC + 1.87BC + 0.23A^2 - 3.12B^2 + 0.98C^2,$$

where A, B, C, and Y represent the concentration of the sample, laser irradiation time, power of laser irradiation, and temperature, respectively. The positive and negative signs indicate synergistic and antagonistic effects on the factors, respectively. Coefficients with single factors represent the effect of that factor, whereas coefficients with two factors and second-order variables represent the effects of interaction among those factors and quadratic nature, respectively. The above equation depicts that the power of the laser has the highest impact, followed by the irradiation time and concentration of the sample on the photothermal transduction potential of the FF-BSC NPs.

A 3D plot was constructed by setting the laser power at 650 mW for the response and temperature (Fig. 3a). Furthermore, numerical and graphical optimization was carried out, and parameters were selected to maintain a temperature of 52–60 °C (Fig. 3b). The design space was validated by selecting three random points, and the experimental results were consistent with the predicted ranges (Table S4).

Photothermal conversion efficacy (PCE)

PCE denotes the potential of FF-BSC NPs to convert absorbed NIR light to heat and is related to the NIR absorption of the material. The PCE of FF-BSC NPs was evaluated under the experimental conditions described (ESI: Section 1.8). The PCE of the FF-BSC NPs was 56.6%, indicating excellent conversion efficacy, and the time vs. temperature was profiled (Fig. 3c, d).
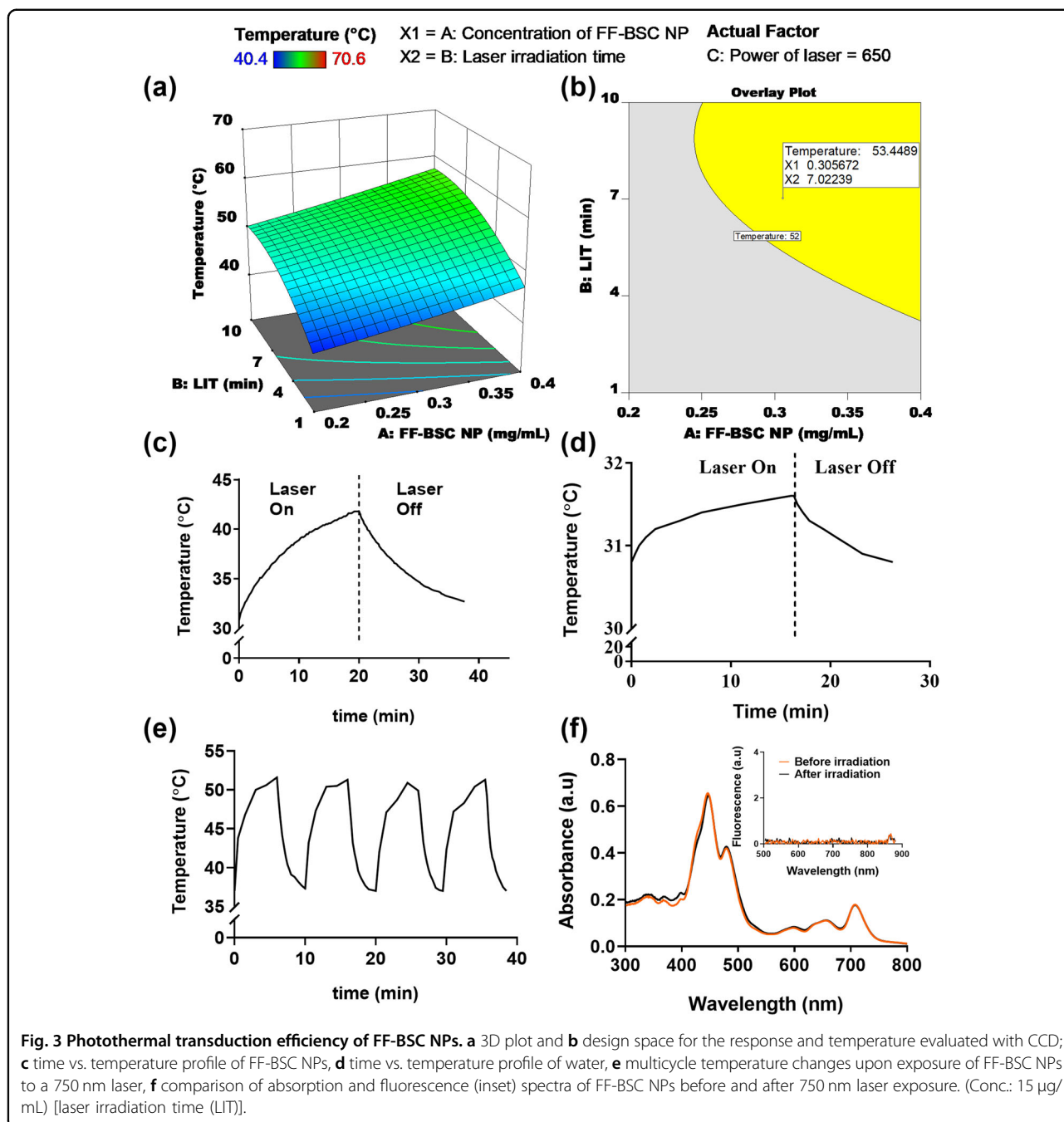
Fig. 3 Photothermal transduction efficiency of FF-BSC NPs. a 3D plot and **b** design space for the response and temperature evaluated with CCD; **c** time vs. temperature profile of FF-BSC NPs, **d** time vs. temperature profile of water, **e** multicycle temperature changes upon exposure of FF-BSC NPs to a 750 nm laser, **f** comparison of absorption and fluorescence (inset) spectra of FF-BSC NPs before and after 750 nm laser exposure. (Conc.: 15 µg/mL) [laser irradiation time (LIT)].

Multicycle photothermal efficacy

To evaluate the photostability and multicycle photothermal potential of FF-BSC NPs, cyclic laser ON/OFF experiments were performed. The photothermal potential of the material was retained even after four laser ON/OFF cycles, and the temperature increment was consistent in every cycle (Fig. 3e). Furthermore, the absorption and fluorescence spectra did not reveal any changes, as shown in Fig. 3f, indicating the stability of the nanomaterial. This is particularly important, as most of the commercially

available dyes, including indocyanine green, are highly sensitive to light[39]. The excellent photothermal properties, coupled with high conversion efficiency (Table S5), and admirable photostability of FF-BSC NPs make them ideal candidates for PTT.

In vitro biocompatibility and hemocompatibility study

External agents such as nanoparticles should be biocompatible to be further utilized as therapeutic agents. Assessment of the in vitro biocompatibility of FF-BSC
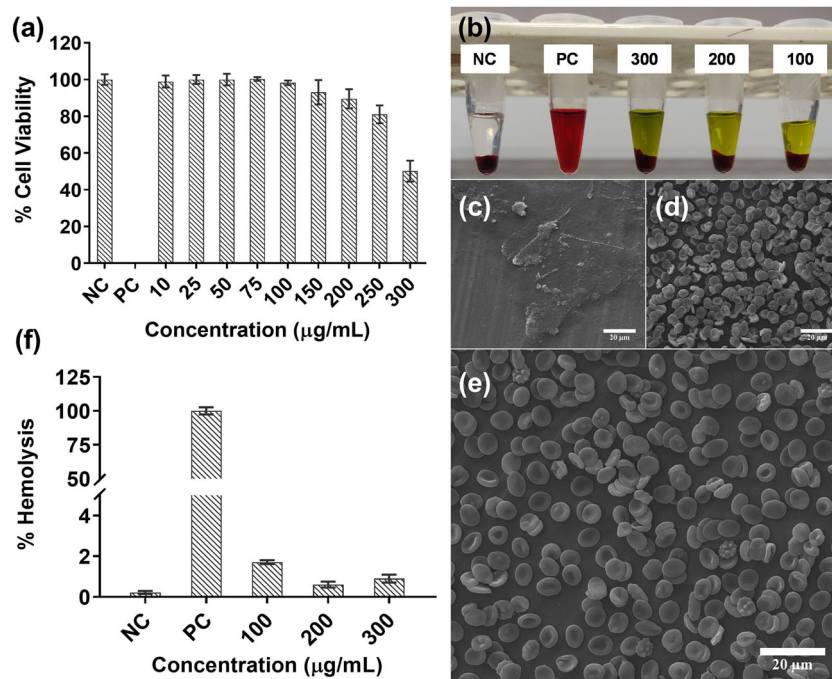
Fig. 4 Biocompatibility and hemocompatibility studies of FF-BSC NPs. a In vitro biocompatibility of FF-BSC NPs in L929 cells, **b** digital image of various samples of hemocompatibility study (FF-BSC NPs in µg/mL), ESEM images of RBCs treated with **c** Triton X-100 (positive control: PC), **d** PBS (negative control: NC), **e** 300 µg/mL FF-BSC NPs, and **f** graph depicting the hemocompatibility study of FF-BSC NPs.
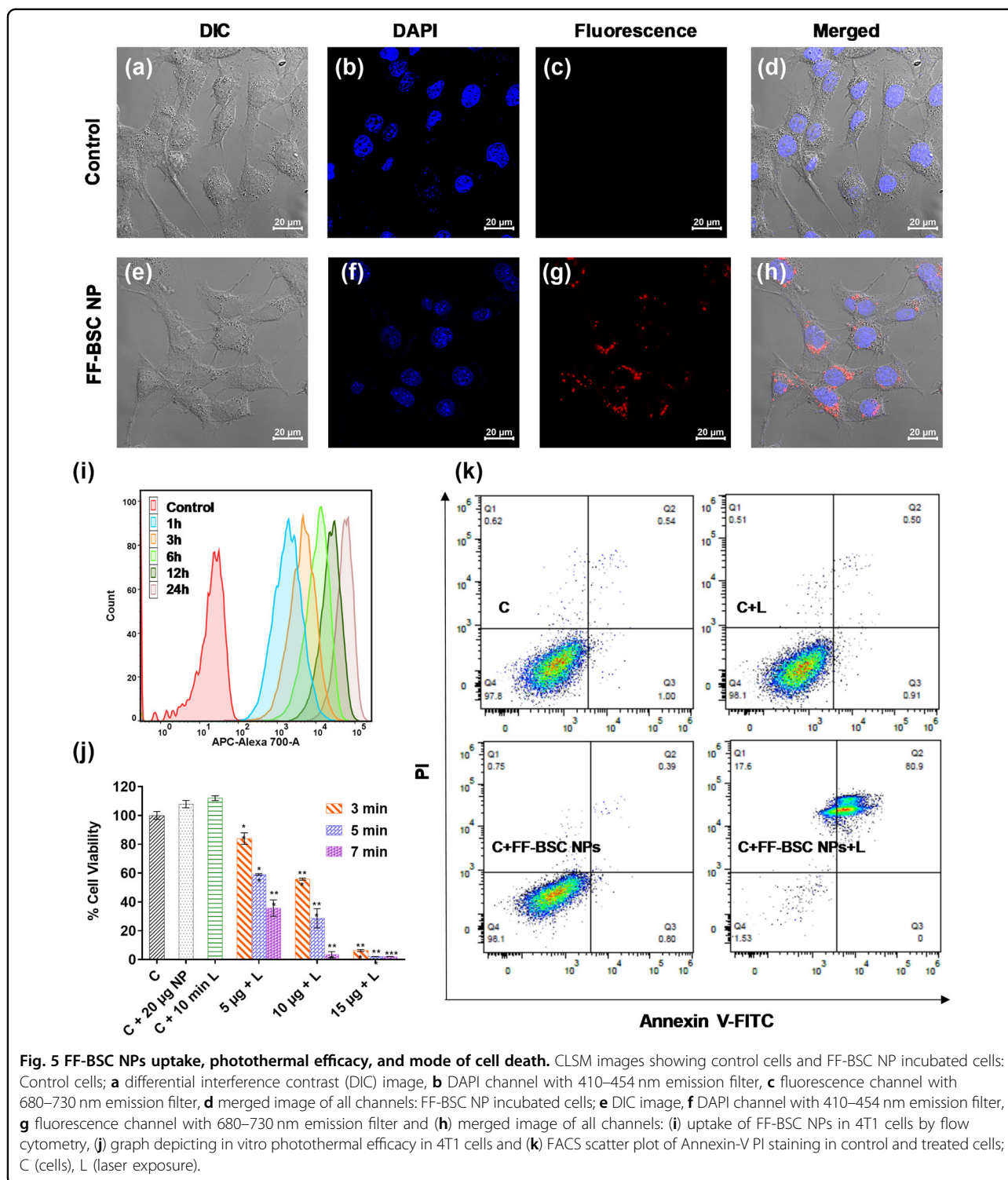
NPs was carried out in L929 cells. A fluorescence-based Alamar blue assay was performed wherein viable cells convert nonfluorescent blue-colored resazurin to fluorescent red-colored resorufin. Evaluation of the fluorescence intensity to determine the percent cell viability revealed that FF-BSC NPs were biocompatible up to a concentration of 250 µg/mL. This result indicated that these nanoparticles possess excellent biocompatibility within the desired therapeutic concentration (Fig. 4a).

The FF-BSC nanoparticulate formulation is expected to encounter blood upon intravenous administration. Hence, the assessment of hemocompatibility is an absolute requirement. Hemo-incompatibility is often influenced by the physicochemical properties of a material, e.g., size, charge, and shape[44]. The blood sample treated with Triton X-100 resulted in complete hemolysis, and no RBC pellet was observed. However, FF-BSC NP treated RBCs did not show any hemolysis (similar to the negative control), as shown in Fig. 4b. Furthermore, ESEM analysis of FF-BSC NP treated samples revealed that the morphology of RBCs was intact, and no significant difference was observed with respect to negative control, however RBCs were completely ruptured in case of positive control (Fig. 4c–e). As mentioned, RBCs treated with varying concentrations of FF-BSC NPs did

not exhibit hemolysis, and the percentage of hemolysis was well below 5%, in accordance with the guidance of American Society for Testing and Materials (ASTM) E2524 (Fig. 4f).

Cellular uptake, photothermal efficacy testing, and mode of cell death

The optimal uptake of nanoparticles by the cells is a crucial factor, as inefficient uptake can compromise the therapeutic efficacy. Hence, the cellular uptake of FF-BSC NPs was rigorously evaluated in 4T1 (murine breast cancer) cells. Confocal laser scanning microscopy (CLSM) revealed that FF-BSC NPs were sufficiently internalized and that the NIR fluorescence of the nanoparticles (680–740 nm) can be efficiently utilized for cellular imaging. Furthermore, DAPI staining experiments confirmed that the FF-BSC NPs were localized in the cytoplasm of the cells (Fig. 5a–h). Additional validation of nanoparticle uptake by the cells was performed with flow cytometry at different time points in 4T1 cells. Flow cytometric analysis indicated that time-dependent uptake of nanoparticles by the cells occurred, starting as early as 1 h; this was evident from the shift in the median fluorescence intensity peak of the NPs incubated cells with respect to the control cells. Following 12–24 h of incubation, NPs internalization was found to be almost 100% of that observed in the control

Fig. 5 FF-BSC NPs uptake, photothermal efficacy, and mode of cell death. CLSM images showing control cells and FF-BSC NP incubated cells: Control cells; **a** differential interference contrast (DIC) image, **b** DAPI channel with 410–454 nm emission filter, **c** fluorescence channel with 680–730 nm emission filter, **d** merged image of all channels: FF-BSC NP incubated cells: **e** DIC image, **f** DAPI channel with 410–454 nm emission filter, **g** fluorescence channel with 680–730 nm emission filter and (**h**) merged image of all channels: (**i**) uptake of FF-BSC NPs in 4T1 cells by flow cytometry, (**j**) graph depicting in vitro photothermal efficacy in 4T1 cells and (**k**) FACS scatter plot of Annexin-V PI staining in control and treated cells; C (cells), L (laser exposure).

cells (Fig. 5i). The efficient fluorescence and uptake of the NPs displayed by the cells after incubation forms the basis for the utilization of these nanoassemblies for further in vitro and in vivo efficacy and whole-body imaging studies.

In vitro therapeutic efficacy evaluation is a prerequisite for in vivo efficacy testing. Thus, in vitro photothermal efficacy testing of FF-BSC NPs was carried out in 4T1 cells. A combination of different nanoparticle concentrations (5, 10, and 15 μg of NPs) coupled with varied
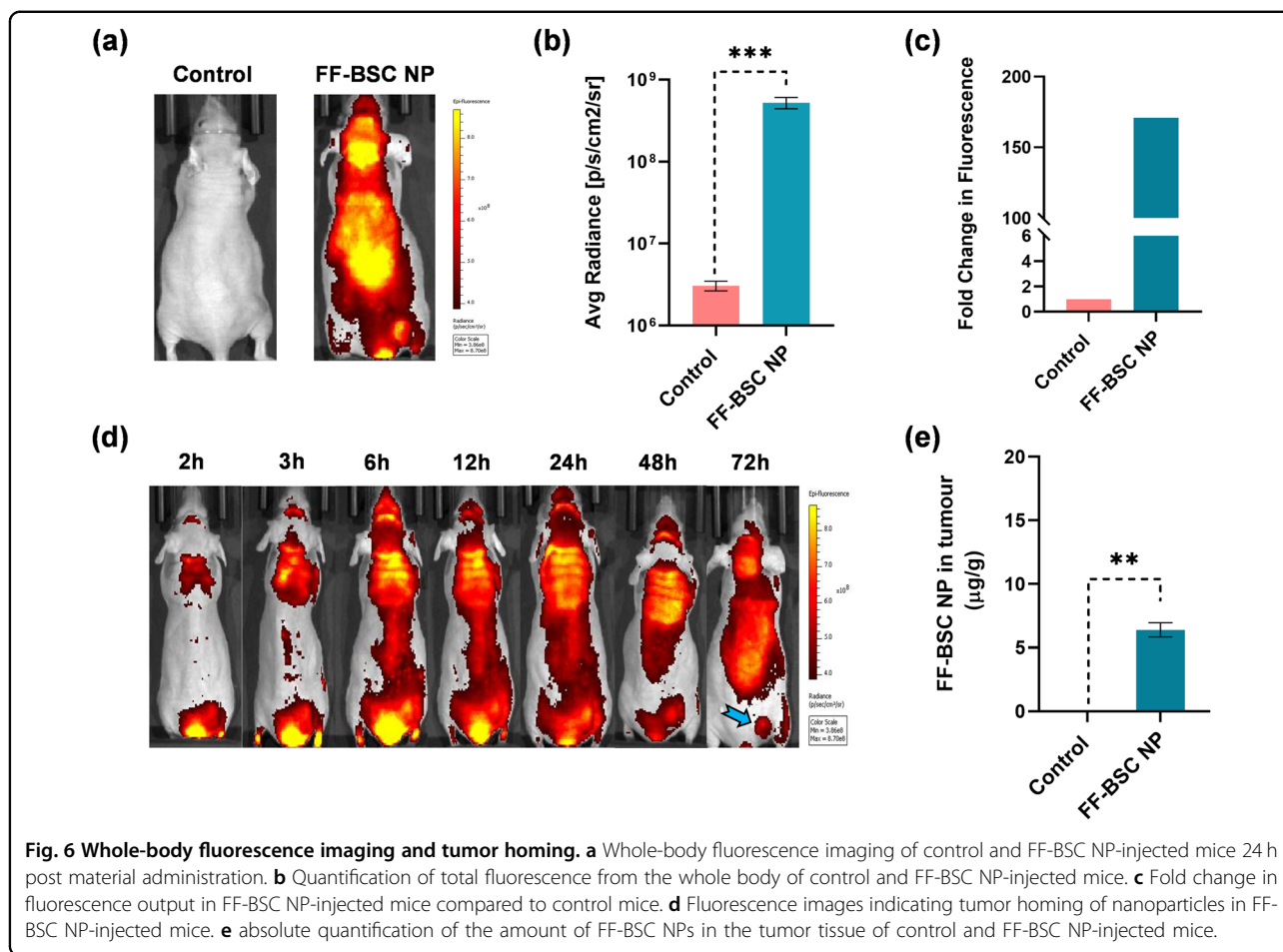
Fig. 6 Whole-body fluorescence imaging and tumor homing. a Whole-body fluorescence imaging of control and FF-BSC NP-injected mice 24 h post material administration. **b** Quantification of total fluorescence from the whole body of control and FF-BSC NP-injected mice. **c** Fold change in fluorescence output in FF-BSC NP-injected mice compared to control mice. **d** Fluorescence images indicating tumor homing of nanoparticles in FF-BSC NP-injected mice. **e** absolute quantification of the amount of FF-BSC NPs in the tumor tissue of control and FF-BSC NP-injected mice.
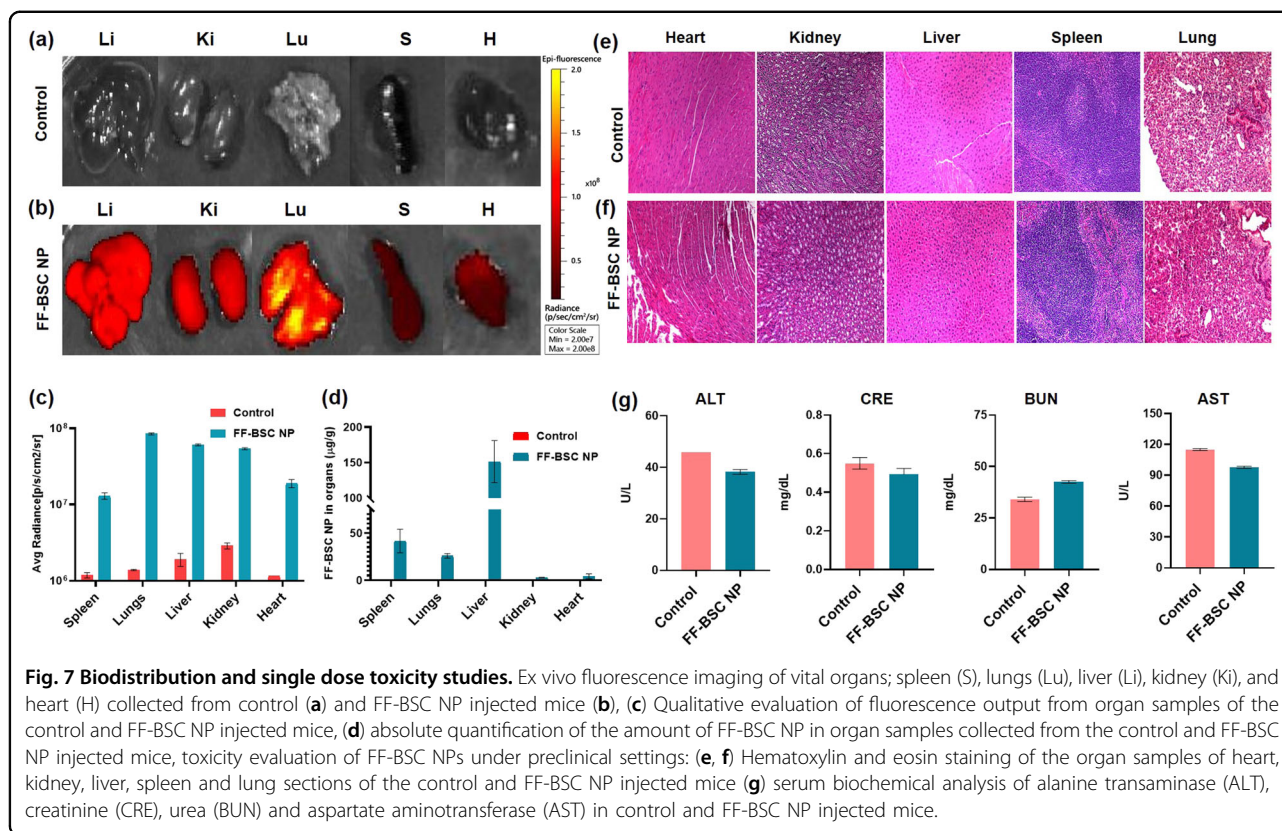
laser exposure durations (3, 5, and 7 min) revealed that 5 μg of NPs and seven min of laser exposure reduced cell viability by more than 50%, as evaluated by the Alamar assay. Increasing the nanoparticle concentration to 10 μg showed a dose-dependent increase in cytotoxicity even at lower laser exposure times (i.e., viability was <40% at 5 min of laser exposure). A further increase in the FF-BSC NP concentration to 15 μg enabled reduced laser exposure (3 min) to be utilized with cell death enhanced to >90% ($p = 0.0002$). Cells exposed to NPs and laser alone did not exhibit changes in cell viability (>95%), (Fig. 5j). Hence, the in vitro study revealed that the developed formulation has excellent photothermal ablation efficacy and potential for in vivo tumor ablation.

Apoptosis-inducing therapeutic agents are clinically preferred, as apoptosis is regarded as a cleaner mechanism of cell death than necrosis, which might induce non-specific inflammation. Gold standard Annexin-V PI staining was performed to determine the mode of cell death after photothermal treatment with FF-BSC NPs. Fractional positivity for Annexin-V, PI single staining, and Annexin-V PI dual staining was observed across all control groups (cells only, cells + laser, cells + FF-BSC NP),

as expected, indicating basal cell death. On the other hand, the PTT treatment group showed a > 80% increase in the dual-stained population and a 17% increase in the PI-stained population, indicating that the majority of cells were in the late apoptotic stage, while a second fraction of the treated population was undergoing necrosis (Fig. 5k). This suggests that PTT using FF-BSC NPs induces a relatively clean mechanism of cell death with little evidence of necrosis, making the treatment procedure using the designed formulation more appealing for clinical application.

Whole-body imaging and in vivo tumor homing

Steady-state photophysical studies revealed severe quenching of fluorescence upon the formation of FF-BSC NPs (Fig. 1c), but significant residual fluorescence was observed in H_2O (Fig. S32), which was sufficient for cellular imaging (Fig. 5a–h). This provides a very strong basis for the possible utilization of FF-BSC NPs as a whole-body imaging agent. In this context, noninvasive live animal fluorescence imaging was performed after intravenous (IV) administration of the nanoformulation in mice. At 24 h after administration, significantly ($p = 0.0001$) strong

Fig. 7 Biodistribution and single dose toxicity studies. Ex vivo fluorescence imaging of vital organs; spleen (S), lungs (Lu), liver (Li), kidney (Ki), and heart (H) collected from control (**a**) and FF-BSC NP injected mice (**b**), (**c**) Qualitative evaluation of fluorescence output from organ samples of the control and FF-BSC NP injected mice, (**d**) absolute quantification of the amount of FF-BSC NP in organ samples collected from the control and FF-BSC NP injected mice, toxicity evaluation of FF-BSC NPs under preclinical settings: (**e**, **f**) Hematoxylin and eosin staining of the organ samples of heart, kidney, liver, spleen and lung sections of the control and FF-BSC NP injected mice (**g**) serum biochemical analysis of alanine transaminase (ALT), creatinine (CRE), urea (BUN) and aspartate aminotransferase (AST) in control and FF-BSC NP injected mice.

fluorescence could be seen throughout the body of the mice, which was >100-fold higher than the background body signal. This clearly suggests that such material holds very strong potential for further exploration as a targeted imaging agent (Fig. 6a–c). Additionally, a desirable feature of any novel nontargeted nanoformulation is the capacity to passively accumulate in tumor tissue, taking advantage of the leaky tumor vasculature *via* the enhanced permeability and retention (EPR) effect. As FF-BSC NPs exhibited sufficient fluorescence, the tumor homing ability of FF-BSC NPs was evaluated by qualitative time-dependent fluorescence imaging. FF-BSC NPs exhibited fluorescence throughout the body during the initial time points (from 2–24 h), as seen from fluorescence imaging. However, after 24 h, at 48 and 72 h, specific homing of a portion of nanoparticles was observed in the tumor (Fig. 6d). Furthermore, to investigate the amount of material accumulated, the tumor tissue was harvested, snap frozen, and homogenized and the compound was extracted in DMSO. The fluorescence of the extract was recorded, and the amount of FF-BSC was quantified. Absolute quantification clearly indicated that out of 300 μg of the FF-BSC NPs injected, a portion (6–7 μg/g) of the compound was deposited in the tumor tissue (Fig. 6e). Although the accumulated quantity was significant ($p = 0.001$), it may not be sufficient for effective

photothermal tumor ablation *via* IV administration of the nanomaterial. Hence, photothermal ablation studies in the preclinical setting were performed with intratumoral injection of FF-BSC NPs.

Biodistribution and single-dose toxicity testing

A detailed understanding of the in vivo biodistribution and toxicity of the FF-BSC NPs in preclinical animal models such as mice, which possess close physiological resemblance to humans, is imperative. Biodistribution and toxicity assessments of FF-BSC NPs were carried out by IV administration of the nanoformulation in swiss mice. Fourteen days after the administration of FF-BSC NPs, ex vivo fluorescence imaging of vital organs, such as the lungs, liver, kidney, spleen, and heart, was performed, indicating the deposition of a majority of the nanoparticles in these organs (Fig. 7a–c). Absolute quantification of the material deposited in these vital organs was also performed by extracting the compound from tissue homogenate in DMSO. The analysis indicated that a larger portion of nanoparticles accumulated in the liver, lung, and spleen, and a lesser quantity accumulated in the kidney and heart (Fig. 7d). These results suggested that the majority of the injected material could not avoid opsonization by the components of the reticuloendothelial system (RES). This hypothesis also accounts for the
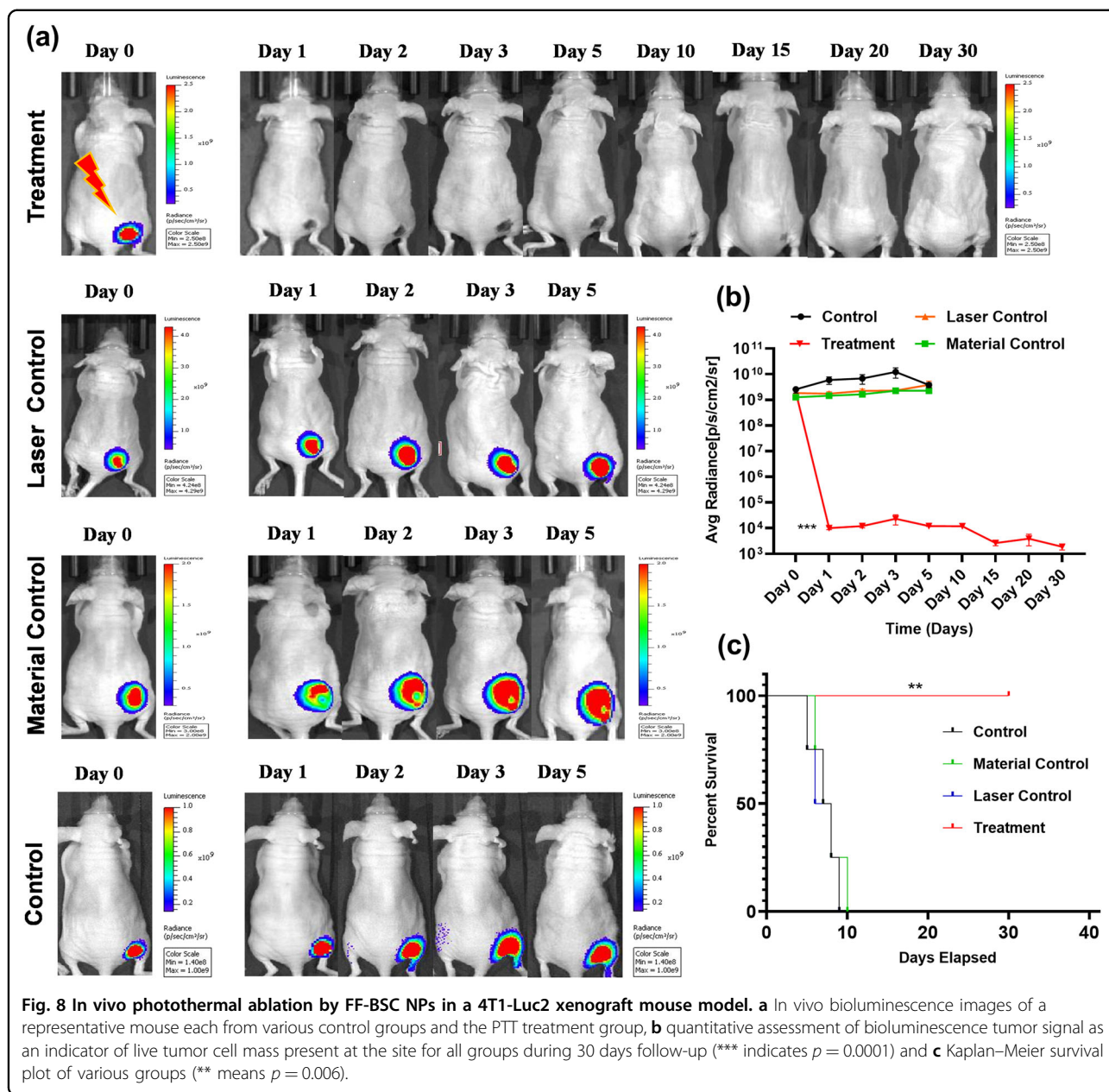
Fig. 8 In vivo photothermal ablation by FF-BSC NPs in a 4T1-Luc2 xenograft mouse model. a In vivo bioluminescence images of a representative mouse each from various control groups and the PTT treatment group, **b** quantitative assessment of bioluminescence tumor signal as an indicator of live tumor cell mass present at the site for all groups during 30 days follow-up (*** indicates $p = 0.0001$) and **c** Kaplan–Meier survival plot of various groups (** means $p = 0.006$).

inefficient passive tumor homing observed in this study. The data also correlate with the ex vivo fluorescence imaging data, further confirming the deposition of the injected compound in these organs. The presence of a portion of injected material in the kidney also hints at the possibility of renal clearance of FF-BSC NPs. Furthermore, histological examination of H&E (hematoxylin and eosin)-stained sections of vital organs showed no visible pathological changes in these organs compared to normal tissues (Fig. 7e, f). Additionally, the acute toxicity of the injected material was evaluated by serum biochemical analysis 72 h after nanomaterial injection. Biochemical analysis revealed that the serum levels of alanine transaminase, aspartate aminotransferase, creatinine, and urea (a key determinant of the normal functioning of liver and kidney) in the material-injected mice were in line with those in the control mice (Fig. 7g). Hence, the formulated NPs are highly biocompatible and nontoxic in these preclinical settings. These encouraging preclinical datasets on FF-BSC NPs will serve the purpose of fast track bench-to-bedside translation of this perspective material.

In vivo photothermal ablation efficacy of FF-BSC NPs

The in vivo photothermal efficacy of FF-BSC NPs was tested in a 4T1-Luc2 xenograft breast tumor model using noninvasive bioluminescence imaging in mice. FF-BSC NPs

(300 μg) were injected intratumorally, which could be a more relevant strategy for the local application of PTT in a clinical setting. Upon exposure to a NIR laser beam at the tumor site, the material showed excellent efficacy in vivo. In comparison to the control groups, a dramatic reduction in bioluminescence signal post PTT ($p = 0.0001$) indicated drastic tumor mass ablation, which was further associated with no signs of weight loss, suggesting minimal or no therapy burden. However, the bioluminescence signal of the control, laser control, and material control groups showed a progressive increase until day 5, indicating the nontoxic nature of the laser/material used in those sets of mice. After day 5, the bioluminescence signal for these groups reached saturation of the CCD camera detection capacity; therefore, beyond this time point, no further imaging was carried out for these animals. However, the animals were followed for survival analysis. Owing to permissible tumor size limitations as well as progressive tumor necrosis beyond day 5, the mice in these groups were killed by day 10. The PTT-treated group of animals was followed up until day 30 and showed no enhancement in the bioluminescence signal (the signal at the ablated tumor site was equivalent to the background), highlighting effective and complete tumor ablation and the lack of signs of tumor relapse post-PTT. This effect prolonged the overall survival of mice in the PTT-treated group (Fig. 8a–c). Altogether, the in vivo data sufficiently indicate the biocompatibility, NIRF imaging potential, and preclinical photothermal efficacy of FF-BSC nano self-assemblies.

Conclusion

Herein, we successfully demonstrated the synthesis of diphenylalanine-conjugated BF_2-oxasmaragdyrin and its self-assembly into spherical nanoparticles. These self-assemblies have shown excellent thermal stability and resistance to photobleaching upon repeated NIR laser exposure. NIRF exhibited by the self-assemblies was efficiently utilized to evaluate organ and tumor distribution kinetics by noninvasive whole-body imaging. The synthesized nanoassemblies displayed efficient cellular uptake and excellent cancer cell ablation in vitro. Furthermore, in vivo studies demonstrated the photothermal efficacy of FF-BSC NPs in 4T1 tumor-bearing mice, resulting in total depletion of tumor growth with a single photothermal treatment cycle (5 min irradiation with a 750 nm laser at 800 mW). The self-assemblies also did not induce any overt or covert toxic effects upon IV administration in mice, clearly highlighting the biocompatible nature of the designed formulation. Altogether, this novel organic nanomaterial holds promise for theragnostic nanomedicine applications by combining sensitive NIRF imaging guidance and photonic hyperthermia-mediated cancer ablation as its prospect in real-life situations.

Author details
[1]IITB-Monash Research Academy, Indian Institute of Technology Bombay, Powai, Mumbai 400076, India. [2]Department of Chemistry, Indian Institute of Technology Bombay, Powai, Mumbai 400076, India. [3]School of Chemistry (Building 23, Room 114C), Monash University, Wellington Road Clayton, Melbourne, Victoria 3800, Australia. [4]Department of Biosciences and Bioengineering, Indian Institute of Technology Bombay, Powai, Mumbai 400076, India. [5]Molecular Functional Imaging Laboratory, ACTREC, Tata Memorial Centre, Kharghar, Navi Mumbai 410210, India. [6]Department of Life Sciences, Homi Bhabha National Institute, BARC Training School Complex, Anushaktinagar, Mumbai 400094, India

Author contributions
M.R., A.D., R.S., and A.R., conceived the idea; K.L., B.P.K.R., S.K.M., M.R., A.D., R.S., and A.R. contributed to the experimental design; K.L., B.P.K.R., and S.K.M., performed the experiments and analyzed the data; K.L., B.P.K.R., and S.K.M. performed statistical analysis; M.R., A.D., R.S., A.R., K.L., B.P.K.R., and S.K.M. reviewed the data and prepared the manuscript. K.L., B.P.K.R., S.K.M. contributed equally.

Conflict of interest
The authors declare that they have no conflict of interest.

Publisher's note
Springer Nature remains neutral with regard to jurisdictional claims in published maps and institutional affiliations.

Supplementary information is available for this paper at https://doi.org/10.1038/s41427-020-00256-x.

References
1. Bray, F. et al. Global cancer statistics 2018: GLOBOCAN estimates of incidence and mortality worldwide for 36 cancers in 185 countries. *Ca. Cancer J. Clin.* **68**, 394–424 (2018).
2. Vines, J. B., Yoon, J. H., Ryu, N. E., Lim, D. J. & Park, H. Gold nanoparticles for photothermal cancer therapy. *Front. Chem.* **7**, 167–182 (2019).
3. Lal, S., Clare, S. E. & Halas, N. J. Nanoshell-enabled photothermal cancer therapy: impending clinical impact. *Acc. Chem. Res.* **41**, 1842–1851 (2008).
4. Abadeer, N. S. & Murphy, C. J. Recent progress in cancer thermal therapy using gold nanoparticles. *J. Phys. Chem. C* **120**, 4691–4716 (2016).
5. Dickerson, E. B. et al. Gold nanorod assisted near-infrared plasmonic photothermal therapy (PPTT) of squamous cell carcinoma in mice. *Cancer Lett.* **269**, 57–66 (2008).
6. Yang, K. et al. Graphene in mice: ultrahigh in vivo tumor uptake and efficient photothermal therapy. *Nano Lett.* **10**, 3318–3323 (2010).
7. Robinson, J. T. et al. Ultrasmall reduced graphene oxide with high near-infrared absorbance for photothermal therapy. *J. Am. Chem. Soc.* **133**, 6825–6831 (2011).
8. Tao, W. et al. Black phosphorus nanosheets as a robust delivery platform for cancer theranostics. *Adv. Mater.* **29**, 1603276 (2017).
9. Zhao, Z., Shi, S., Huang, Y., Tang, S. & Chen, X. Simultaneous photodynamic and photothermal therapy using photosensitizer-functionalized Pd nanosheets by single continuous wave laser. *ACS Appl. Mater. Interfaces* **6**, 8878–8885 (2014).

10. Zhou, M. et al. CuS nanodots with ultrahigh efficient renal clearance for positron emission tomography imaging and image-guided photothermal therapy. *ACS Nano* **9**, 7085–7096 (2015).

11. Hessel, C. M. et al. Copper selenide nanocrystals for photothermal therapy. *Nano Lett.* **11**, 2560–2566 (2011).

12. Song, G. et al. Hydrophilic molybdenum oxide nanomaterials with controlled morphology and strong plasmonic absorption for photothermal ablation of cancer cells. *ACS Appl. Mater. Interfaces* **6**, 3915–3922 (2014).

13. Yang, J. et al. Convertible organic nanoparticles for near-infrared photothermal ablation of cancer cells. *Angew. Chem. Int. Ed.* **50**, 441–444 (2010).

14. Yu, J. et al. Self-assembly synthesis, tumor cell targeting, and photothermal capabilities of antibody-coated indocyanine green nanocapsules. *J. Am. Chem. Soc.* **132**, 1929–1938 (2010).

15. Feng, G., Liu, J., Geng, J. & Liu, B. Conjugated polymer microparticles for selective cancer cell image-guided photothermal therapy. *J. Mater. Chem. B* **3**, 1135–1141 (2015).

16. Cheng, L., Wang, C., Feng, L., Yang, K. & Liu, Z. Functional nanomaterials for phototherapies of cancer. *Chem. Rev.* **114**, 10869–10939 (2014).

17. Kobayashi, H., Ogawa, M., Alford, R., Choyke, P. L. & Urano, Y. New strategies for fluorescent probe design in medical diagnostic imaging. *Chem. Rev.* **110**, 2620–2640 (2010).

18. Fischer, G. M., Isomäki-Krondahl, M., Göttker-Schnetmann, I., Daltrozzo, E. & Zumbusch, A. Pyrrolopyrrole cyanine dyes: a new class of near-infrared dyes and fluorophores. *Chem. – A Eur. J.* **15**, 4857–4864 (2009).

19. Arunkumar, E., Forbes, C. C., Noll, B. C. & Smith, B. D. Squaraine-derived rotaxanes: sterically protected fluorescent near-IR dyes. *J. Am. Chem. Soc.* **127**, 3288–3289 (2005).

20. Umezawa, K., Nakamura, Y., Makino, H., Citterio, D. & Suzuki, K. Bright, color-tunable fluorescent dyes in the visible—near-infrared region. *J. Am. Chem. Soc.* **130**, 1550–1551 (2008).

21. Loudet, A. et al. B, O-chelated azadipyrromethenes as near-IR probes. *Org. Lett.* **10**, 4771–4774 (2008).

22. Yang, Y. et al. Seminaphthofluorones are a family of water-soluble, low molecular weight, NIR-emitting fluorophores. *Proc. Natl Acad. Sci. U. S. A.* **105**, 8829–8834 (2008).

23. Nesterova, I. V. et al. Metallo-phthalocyanine near-IR fluorophores: oligonucleotide conjugates and their applications in PCR assays. *Bioconjug. Chem.* **18**, 2159–2168 (2007).

24. Kuimova, M. K. et al. Photophysical properties and intracellular imaging of water-soluble porphyrin dimers for two-photon excited photodynamic therapy. *Org. Biomol. Chem.* **7**, 889–896 (2009).

25. Xie, D. et al. Meso-triaryl-substituted smaragdyrins: facile aromaticity switching. *J. Am. Chem. Soc.* **140**, 16553–16559 (2018).

26. Narayanan, S. J., Sridevi, B., Chandrashekar, T. K, Englich, U. & Ruhlandt-Senge, K. Core-modified smaragdyrins: first examples of stable meso-substituted expanded corrole. *Org. Lett.* **1**, 587–590 (1999).

27. Chatterjee, T., Srinivasan, A., Ravikanth, M. & Chandrashekar, T. K. Smaragdyrins and sapphyrins analogues. *Chem. Rev.* **117**, 3329–3376 (2017).

28. Rajeswara Rao, M. & Ravikanth, M. Boron complexes of oxasmaragdyrin, a core-modified expanded porphyrin. *J. Org. Chem.* **76**, 3582–3587 (2011).

29. Laxman, K. & Ravikanth, M. Synthesis of oxasmaragdyrin–amino acid conjugates. European. *J. Org. Chem.* **2017**, 5884–5891 (2017).

30. Kalita, H., Lee, W.-Z. & Ravikanth, M. Phosphorus complexes of meso-Triaryl-25-oxasmaragdyrins. *Inorg. Chem.* **53**, 9431–9438 (2014).

31. Laxman, K., Reddy, B. P. K., Robinson, A., Srivastava, R. & Ravikanth, M. Cell-penetrating peptide-conjugated BF 2 -Oxasmaragdyrins as NIRF imaging and photothermal agents. *ChemMedChem*. https://doi.org/10.1002/cmdc.202000401 (2020).

32. Laxman, K., Reddy, B. P. K., Robinson, A., Srivastava, R. & Ravikanth, M. Synthesis and studies of glucosamine conjugated BF2-oxasmaragdyrin. *ChemistrySelect* **5**, 938–943 (2020).

33. Zhao, L., Liu, Y., Xing, R. & Yan, X. Supramolecular photothermal effects: a promising mechanism for efficient thermal conversion. *Angew. Chem. Int. Ed.* **59**, 3793–3801 (2020).

34. Yan, X., Zhu, P. & Li, J. Self-assembly and application of diphenylalanine-based nanostructures. *Chem. Soc. Rev.* **39**, 1877–1890 (2010).

35. Zou, Q. et al. Biological photothermal nanodots based on self-assembly of peptide-porphyrin conjugates for antitumor therapy. *J. Am. Chem. Soc.* **139**, 1921–1927 (2017).

36. Souza, M. I. et al. Conjugation with L,L-diphenylalanine self-assemblies enhances in vitro antitumor activity of phthalocyanine photosensitizer. *Sci. Rep.* **7**, 13166 (2017).

37. Li, S., Zhao, L., Chang, R., Xing, R. & Yan, X. Spatiotemporally coupled photoactivity of phthalocyanine–peptide conjugate self-assemblies for adaptive tumor theranostics. *Chem. A Eur. J.* **25**, 13429–13435 (2019).

38. Hu, J. J., Cheng, Y. J. & Zhang, X. Z. Recent advances in nanomaterials for enhanced photothermal therapy of tumors. *Nanoscale* **10**, 22657–22672 (2018).

39. te Velde, E. A., Veerman, T., Subramaniam, V. & Ruers, T. The use of fluorescent dyes and probes in surgical oncology. *Eur. J. Surgical Oncol.* **36**, 6–15 (2010).

40. Fernandez-Fernandez, A. et al. Comparative study of the optical and heat generation properties of IR820 and indocyanine green. *Mol. Imaging* **11**, 99–113 (2012).

41. Huang, K. et al. IR820 covalently linked with self-assembled polypeptide for photothermal therapy applications in cancer. *Biomater. Sci.* **6**, 2925–2931 (2018).

42. Mane, S. B. et al. Novel expanded porphyrin sensitized solar cells using boryl oxasmaragdyrin as the sensitizer. *Chem. Commun.* **49**, 6882–6884 (2013).

43. Yu, J. & Anchordoquy, T. J. Synergistic effects of surfactants and sugars on lipoplex stability during freeze-drying and rehydration. *J. Pharm. Sci.* **98**, 3319–3328 (2009).

44. Gatoo, M. A. et al. Physicochemical properties of nanomaterials: Implication in associated toxic manifestations. *BioMed. Res. Int.* **2014**, 1–9 (2014).